HHS Public Access

Author manuscript

Neuroimage Rep. Author manuscript; available in PMC 2023 June 29.

Published in final edited form as:

Neuroimage Rep. 2023 June ; 3(2): . doi:10.1016/j.ynirp.2023.100174.

Exploring interhemispheric connectivity using the directional tract density patterns of the corpus callosum

Ali Demir[a,b,*], **H. Diana Rosas**[a,b]

[a]Department of Neurology, Massachusetts General Hospital and Harvard Medical School, Boston, MA, USA

[b]Athinoula A. Martinos Center for Biomedical Imaging, Massachusetts General Hospital and Harvard Medical School, Charlestown, MA, USA

Abstract

The corpus callosum (CC) is one of the most important interhemispheric white matter tracts that connects interrelated regions of the cerebral cortex. Its disruption has been investigated in previous studies and has been found to play an important role in several neurodegenerative disorders. Currently available methods to assess the interhemispheric connectivity of the CC have several limitations: i) they require the *a priori* identification of specific cortical regions as targets or seeds, ii) they are limited by the characterization of only small components of the structure, primarily voxels that constitute the mid-sagittal slice, and iii) they use global measures of microstructural integrity, which provide only limited characterization. In order to address some of these limitations, we developed a novel method that enables the characterization of white matter tracts covering the structure of CC, from the mid-sagittal plane to corresponding regions of cortex, using directional tract density patterns (dTDPs). We demonstrate that different regions of CC have distinctive dTDPs that reflect a unique regional topology. We conducted a pilot study using this approach to evaluate two different datasets collected from healthy subjects, and we demonstrate that this method is reliable, reproducible, and independent of diffusion acquisition parameters, suggesting its potential applicability to clinical applications.

Keywords

Tract density imaging; Interhemispheric connectivity; Corpus callosum; Directional tract density pattern; Diffusion; Magnetic resonance imaging; Human subjects

*Corresponding author. 149 Thirteenth Street, Suite 10134, Charlestown, MA, 02129, USA. ademir@mgh.harvard.edu (A. Demir).

Declaration of competing interest

The authors declare that they have no known competing financial interests or personal relationships that could have appeared to influence the work reported in this paper.

Data/code availability statement

The original contributions presented in the study are included in the article, further inquiries can be directed to the corresponding author. The code and compiled binaries including the graphical user interface for dTDP will be made available to public in here: https://bitbucket.org/_ali_demir/dtdp.

Ethics statement

The studies involving human participants were reviewed and approved by Partners Human Research Committee. The patients/participants provided their written informed consent to participate in this study.

1. Introduction

The integrity of the corpus callosum (CC), the largest of the commissural white matter pathways in the brain, is critical for normal neurological functions. Its disruption has been associated with several neurological diseases, including Alzheimer's, Parkinson's, and Huntington's (Nir et al., 2013; Wu et al., 2020; Rosas et al., 2010), but because of its complex architecture, studies of the CC have been technically challenging. For example, anatomical studies have attempted to use distinct parcellation schemes to obtain thickness and/or volume measures of the CC (Emsell et al., 2017; Rosas et al., 2010). The brain-image atlases that have been used to reconstruct the structure, such as the one proposed by Julich (Amunts et al., 2020) or the Johns Hopkins University diffusion-based white matter atlas (Mori and Crain, 2005) represent an average shape of the CC and require non-linear warping of the average shape to individual images, which pose technical challenges. The Hofer-Frahm scheme (Hofer and Frahm, 2006) identifies five unique CC regions in humans based on the structural connectivity assessed by the diffusion tractography between cortical regions as the fibers pass through the mid-sagittal section. This approach has been used to evaluate differences in callosal topography (Rosas et al., 2010; Stezin et al., 2021; Rusina et al., 2022) and has remained the standard for the anatomical evaluation of the CC. Although its applicability has already been established, that can practically be extended well beyond the mid-sagittal section.

Other studies have instead used diffusion metrics, which characterize microstructural tissue properties including fractional anisotropy (FA), axial diffusivity (AD), and radial diffusivity (RD) (Basser and Pierpaoli, 1996; Kingsley, 2006). In these instances, alterations in microstructural integrity have been typically associated with reductions in FA or increases in RD or AD (Xu et al., 2021), however, while they provide estimations about microstructural integrity, they primarily provide indirect information about macroscopic connectivity. Newer approaches, including the one proposed by Huang et al. (2019), which uses very high diffusion gradients, enable the evaluation of axon diameter/density and have been suggested to be more sensitive and more closely associated with cognitive measures.

Determining interhemispheric connectivity presents an even greater challenge. The interhemispheric connectivity of the CC has been estimated using cortical regions that have been *a priori* identified (Rubinov and Sporns, 2010), but these regions have been defined as both target and source for tractography (Russo et al., 2022), thereby limiting its true evaluation. In addition, the magnitude of the number of fibers traversing through the CC interconnecting cortical regions have been very difficult to deconvolve; available tools are primarily unable to adequately characterize interhemispheric fibers because of the magnitude of the connections that travel through CC. Finally, when seeded from a cortical region, traditional tractography can fail to reach the corresponding region of the opposite hemisphere. To overcome some of these limitations, advanced tools and sophisticated ROI definitions are necessary to delineate and subdivide callosal pathways so that the region of a bundle of CC can be used for tract-specific analysis (Watanabe et al., 2018; Münch et al., 2022).

In this study we developed a novel approach that maintains the information of the orientation and position of fiber trajectories and that allows the quantification of fiber tract density along the entire length of the CC. We hypothesized that anatomically aligned directional tract density patterns were unique for specific regions of the CC and could be used to evaluate regional interhemispheric connectivity without specifying an *a priori* destination. Although more work is needed, our findings using two healthy-subject datasets suggest that this novel analytical algorithm provides an accurate estimation of interhemispheric connectivity that is also reliable, reproducible, independent of diffusion acquisition parameters, and that have the potential to be used to evaluate interhemispheric connectivity in clinical applications.

2. Methods

2.1. Datasets

2.1.1. Synthetic dataset—A synthetic dataset using the Phantomas tool (Caruyer et al., 2014) was generated to provide a simplified reconstruction to evaluate interhemispheric connections, which are often complex due to their branching nature (Schilling et al., 2019). This was intended to evaluate the effect of different acquisition parameters, including angular resolution and gradient strength, on the dTDPs.

The Phantomas tool required inputs of heuristic control points, which were linked in order to form a polynomial trajectory (Fig. 1a) to create a synthetic diffusion dataset that included information regarding bundle size and diffusion acquisition configurations, such as b-values and uniformly oriented gradient b-vectors. Heuristic control points included a smaller bundle running towards the inferior direction with half the radius size of the main CC bundle.

We used three diffusion-weighting schemes: i) b700 with 10 $b = 0$ and 60 (number of orientations) $b = 700 \left[s/mm^2 \right]$ images; ii) b2000 with 3 $b = 0$ and 90 $b = 2000 \left[s/mm^2 \right]$ images; and iii) multi-shell scheme with 6 $b = 0$, 14 $b = 500$, 48 $b = 1000$, and 66 $b = 2000 \left[s/mm^2 \right]$ images. We also used two commonly available diffusion imaging (isotropic) resolutions of 1 and 2 mm to compare the sensitivity of dTDPs to the voxel resolution. In addition, two cross-section bundle sizes (radius of 8 and 12 mm) were used to simulate CC bundles of different sizes. With these input sets, the parameter combination created 12 synthetic diffusion images. A sample output is depicted for the given parameters in Fig. 1 with reconstructed fiber orientation distributions (FODs).

2.1.2. Human datasets—We used two available human datasets. The first was a publicly available comprehensive diffusion MRI dataset (CDMD), which included healthy human subjects ($N = 24$, 15F/9M, mean age 34.0 ± 10.9) scanned on the MGH-USC (Siemens Skyra) 3T Connectome scanner (Tian et al., 2022). This dataset also included a subset of repeated scans ($N = 6$, 3F/3M, mean age 31.3 ± 10.1) from the same participants. A second dataset, the healthy human subjects dataset (HHSD), consisted of scans acquired on Siemens Tim Trio 3T MRI scanner at the A.A. Martinos Center for Biomedical Imaging. This dataset was further subdivided into HHSD-A, which included subjects ($N = 24$, 15F/9M, mean age 34.9 ± 7.6) that were age-matched to the CDMD, and another

group HHSD-B (N = 33, 14F/19M, mean age 45.9 ± 2.7), which allowed us to evaluate the reliability of these measures.

CDMD imaging parameters (Tian et al., 2022): T1-weighted structural MRI data were acquired using an MEMPRAGE sequence with isotropic resolution of 1.0 mm, TR = 2530 ms, TE = {1.15, 3.03, 4.89, 6.75} ms, flip angle = 7°, and TI = 1100 ms. Diffusion weighted data were acquired using multiple b-value shells (50 b = 0 $\lfloor s/mm^2 \rceil$ and 16 different b values ranging from 50 to 17,800 [s/mm^2]), each shell having 32 (for b < 2400 s/mm^2) or 64 (for b ≥ 2400 s/mm^2) diffusion encoding directions. Imaging parameters were set with a = 2 mm (isotropic), TR = 3800 ms, and TE = 77 ms.

HHSD imaging parameters: High resolution MEMPRAGE/T1 image (root-mean-square average of 4 echos) acquired with isotropic resolution of 1.0 mm, TR = 2530 ms, TE = {1.64, 3.5, 5.36, 7.22} ms, flip angle = 7°, and TI = 1200 ms. The diffusion data used 70 diffusion weighted volumes (10 b = 0 $\lfloor s/mm^2 \rceil$ and 60 b = 700 $\lfloor s/mm^2 \rceil$ images), isotropic resolution of 2 mm, TR = 7980 ms, and TE = 83 ms.

2.2. Data pre-processing framework

Synthetic dataset: Diffusion-weighted images were first denoised (Veraart et al., 2016) and FODs were reconstructed using a constrained spherical deconvolution model. For single-shell data, we used a Turnier response function estimation, and for the multi-shell data, we used the 'dhollander' option (Dhollander et al., 2019) for the response function estimation because the 5tt algorithm expects the diffusion data to include brain structures that do not exist in the synthetic dataset. For the two different bundle size configurations, a mid-sagittal cross section of the mean b0 images was used to draw a manual seed region, which imitated the CC cross section segmentation step performed for the human datasets.

CDMD: Processing steps were described in Tian et al. (2022). For the diffusion model fitting we used MRtrix3[1] pipeline using b = 800, 1500, 2400, 3450 s/mm^2 shells. Since the CDMD was multi-shell diffusion acquisition, we used the multi-shell-multi-tissue options for both the response function estimation and FOD reconstruction steps.

HHSD: The diffusion images were denoised (Veraart et al., 2016) and corrected for distortion using FSL FUGUE (Jenkinson et al., 2012) before correcting for eddy currents and head motions using FSL Eddy (Andersson and Sotiropoulos, 2016; Andersson et al., 2016). White matter FODs were obtained using a constrained spherical deconvolution model with a Turnier response function estimation using MRtrix3. Tract density images were reconstructed using (Calamante et al., 2010) to evaluate the white matter integrity of CC with *IFOD2* probabilistic tractography (Tournier et al., 2007, 2010; Jeurissen et al., 2014).

Anatomical reconstruction and registration: We used FreeSurfer[2] (version 7) to form an initial mask of the CC for the human datasets. Each individual T1 image was rigidly

[1] mrtrix.org.
[2] surfer.nmr.mgh.harvard.edu.

registered using FSL Flirt (rotation and translation) to the MNI152 (Mazziotta et al., 2001) standard space so that all subjects had a unified brain tilt along the AC-PC line. Diffusion weighted images were co-registered to the T1 image using a boundary-based registration (Greve and Fischl, 2009). Using the estimated registration matrices, the tract density maps were transformed to MNI152 space.

2.3. Segmentation and parcellation of the corpus callosum

The CC labels (251–255) from the FreeSurfer reconstruction were binarized to form a CC mask, which served as a boundary condition for the CC segmentation. The principal direction of diffusion ($V1$) and fractional anisotropy (FA) maps were utilized as factors for the CC curve evolution and segmentation of CC, for which $V1$ is expected to align in right to left direction ([1, 0, 0]) and FA is expected to be lower beyond the CC. The mid-sagittal slice was first located using the user interface along the sagittal slices, and then central voxels of the genu ($\overrightarrow{c_1}$) at the most anterior aspect of the structure (Fig. 2a), and the splenium ($\overrightarrow{c_n}$) at the most posterior aspect (Fig. 2b) were identified. Using Algorithm 1, we reconstructed a centerline CC curve by following a direction with the maximum metric ω towards the direction of interest, $\overrightarrow{d_i}$ as shown in Fig. 2 using an adapted version of the Hofer-Frahm CC parcellation scheme to label the arcs of the CC curve as I, IIa, IIb, III, IV, and V in the order starting from the genu (I) to the splenium (V), as shown in Fig. 2d. Neighboring voxels of the curve were included in the parcellation using a modified version of the metric ω of the Algorithm 1, as given in Equation (1)[3], if a certain threshold criteria ($\omega' > \delta$) was met. The green regions shown in Fig. 2(a, b, and c) depict the voxels which met $\omega' > \delta$ condition. The threshold parameter δ was chosen heuristically as 0.15 to include all white matter voxels for seeding the tract.

$$\omega' = CC_{recon}(\overrightarrow{x})FA(\overrightarrow{x})\langle V1(\overrightarrow{x}),\ [1,\ 0,\ 0]\rangle \tag{1}$$

2.4. Tractography seeding and tract density imaging

The fiber tractography from each CC region was initiated using 50000 seeds to densely cover the entire region, respectively. The *IFOD2* probabilistic tractography algorithm (Tournier et al., 2010) was used to reconstruct fiber pathways using the white matter mask obtained from 5ttgen script of the MRtrix as the mask to generate a border at which to terminate the tracts. Track density maps (Calamante et al., 2010) were reconstructed to measure the density of interhemispheric bundles traversing through each of the six regions of the CC (shown in Fig. 3).

2.5. Definition of a projection plane for tract density images

$D(\overrightarrow{X})$ was defined as the mapping from $\mathbb{R}^3$ to $\mathbb{R}$, to show tract density for a voxel coordinate $\overrightarrow{X} \in \mathbb{R}^3$, and $\overrightarrow{j}$ be the unit vector, which runs as depicted in Fig. 4a towards the normal vector to the tangent of the CC curve at the centroid of the CC region, $\overrightarrow{c_s}$. We defined

[3]For the neighbor inclusion metric, $\langle,\rangle$ denotes the dot product and $\overrightarrow{x}$ is a voxel along the perpendicular direction to the tangent of the curve.

the projection plane, **P**, by rotating the coronal image plane, for which the normal vector was [0, 1, 0], towards the anterior, about the origin point $\overrightarrow{c_s}$ and fixed axis $\overrightarrow{i} = [1, 0, 0]$, which was to the left of the brain, so that **P** was defined with $\overrightarrow{c_s}$ and the unit vectors $\overrightarrow{i}$, $\overrightarrow{j}$ and $\overrightarrow{k}$, where $\overrightarrow{i}$ and $\overrightarrow{j}$ on the plane, and $\overrightarrow{k}$ is normal to the plane as depicted in Fig. 4. A Cartesian coordinate space defined on **P**, and for each point on **P**, the tract densities, $D(\overrightarrow{X})$, were integrated along the depth axis ($\overrightarrow{k} = \overrightarrow{i} \otimes \overrightarrow{j}$) of the coordinate point in both towards and the opposite ($-\overrightarrow{k}$) directions to form a projection image $I(\overrightarrow{X}_{(a,b)})$, as depicted in Fig. 4 for the CC regions, showing the projection sum of the tract density at each point ($\overrightarrow{X}_{(a,b)} = \overrightarrow{c_s} + a\overrightarrow{i} + b\overrightarrow{j}$) sampled on **P**, such that $I(\overrightarrow{X}_{(0,0)})$ is located at the origin and shows the sum of the tract densities along the direction of the normal vector at the point $\overrightarrow{c}_s$. Field of view for $I(\overrightarrow{X}_{(a,b)})$ was adjusted large enough to include all brain regions.

2.6. Directional tract density pattern

Once the tract densities were projected and summed on the plane **P** producing an image $I(\overrightarrow{X}_{(a,b)})$, the projection image I was subdivided into equal angular pieces centered at the $\overrightarrow{c_s}$, and the integral of the density values for each angular piece formed a two-dimensional polar function, which we named as the directional tract density pattern (dTDP). Let $Q(k\alpha)$ represent the dTDP function showing the sum of tract densities along each k^{th} angular portion, where $\alpha = 2\pi/K$ is the small delta angle, K is the number of angular portions, and $k \in \{0, 1, 2, \ldots, K-1\}$. First, $Q(k\alpha)$ was initialized to $0.0\ \forall\ k$. Then, all the sampled points $\overrightarrow{X}_{(a,b)}$ on the image $I(\overrightarrow{X}_{(a,b)})$ were iterated, and each tract density value, $I(\overrightarrow{X}_{(a,b)})$, was added to the sum $Q(k\alpha)$, where $k\alpha$ was the corresponding angular portion of (a, b) in polar coordinates. For this study we had $K = 64$ angular portions sampled over 2π. Ultimately, $Q(k\alpha)$ becomes a polar function showing the directional tract densities along the angular portion $(k\alpha)$ thereby forming the dTDP of the CC region.

This is shown in Fig. 5. In this case, we overlaid the dTDP of CC region III on the projection sum image, $I(\overrightarrow{X}_{(a,b)})$, from a healthy subject. We also defined the surface and side lobe of the dTDP, such that surface lobes represent the total density of fibers that traverse to the cortical regions of the brain as identified by Hofer and Frahm (2006), whereas the side lobes represent the total density of tracts traversing from the seeded region to the left and right and that then run towards also the inferior brain regions. Note that dTDP provides an indirect quantification for the interhemispheric connectivity of cortical regions.

2.7. Reliability and variability metrics of dTDPs

To determine the reliability of the dTDPs for the datasets, pairwise dTDPs were evaluated using a Pearson correlation coefficient, and the coefficients of each region was averaged to demonstrate the similarity (score of 1.0 designated that the dTDPs were identical).

In addition, to evaluate between-subject variability between the human datasets, we computed a quartile coefficient of dispersion (QCD) metric (Bonett, 2006) weighted with the

median for the dTDPs using Equation (2), where $\{Q_1^k,\ Q_2^k,\ Q_3^k\}$ are the first quartile, median, and the third quartile of the dTDP values for the given angular portion (k) respectively.

$$QCD = \frac{\sum_{k=0}^{K-1} Q_2^k (Q_3^k - Q_1^k)}{\sum_{k=0}^{K-1} Q_2^k (Q_3^k + Q_1^k)} \tag{2}$$

For the group analysis, we utilized the quartile statistics plotted on the polar coordinate space, such that each angular portion (k) had 25^{th} percentile (1^{st} quartile), median (50^{th} percentile), and 75^{th} percentile (3^{rd} quartile), and the area between the 1^{st} and 3^{rd} quartiles was shaded to show the variability of each dataset. We used a paired t-test to determine if there were significant differences in the density distributions along each angular portion. Since we were mostly interested in inter-hemispheric cortical connectivity, reflected by metrics along the upper directions, we ignored the lower $(\pi/2 < k\alpha < 3\pi/2)K/2$ directions as well as the directions that likely reflect noisy dTDP magnitudes, as observed in central directions $(0,\ \pi/2,\ 3\pi/2)$.

3. Results

3.1. Evaluations of the synthetic dataset: analytical fiber stream

We computed the correlations between pairwise dTDPs obtained for the synthetic CC data, and found that all the pairwise correlations were greater than 0.99, depicted in Fig. 6. We depicted 9 of the dTDPs in Fig. 6, such that each column image represents data from a different gradient orientation scheme. By comparing the first row images to the second row, i.e. Fig. 6a vs. 6d, 6b vs. 6e, and 6c vs. 6f, we observed that changing the voxel resolution did not change the dTDP, irrespective of whether an 8 mm or 12 mm CC radius size was used. The second and third row images (d-i) of Fig. 6 were depicted the patterns for different bundle radius sizes, where the voxel resolution was fixed to 1 mm. To summarize the comparisons, we stacked all the dTDPs in Fig. 6j, k showing the dTDPs overlaid on the same polar space separately for 8 mm and 12 mm bundle sizes. Here, we can observe for the bundle radius size of 12 mm that the given diffusion scheme and image resolution presets produced a synthetic data which had almost identical dTDPs. However, for the bundle size of 8 mm, the multi-shell scheme produced smaller directional tract density compared to the b700 and b2000 scheme for the left and right side lobes of the dTDP; even in this case, the pairwise correlations were greater than 0.99.

3.2. Evaluations of the human datasets

3.2.1. Variability of dTDPs—In Fig. 7, the quartile statistics of dTDP for the CDMD and HHSD-A demonstrated that dTDPs for the two datasets were not significantly different from each other, with the exception of random directions of the CC regions IIa, IIb, III, and IV. The quartile dTDP statistics for the CC regions I and V were also not significantly different for any direction, suggesting that these measures were largely unaffected by the diffusion acquisition parameters.

Fig. 8 depicts the quartile statistics for the HHSD-B dataset providing the normative dTDPs of each CC region. For this dataset, the QCD scores of the CC regions were {0.13, 0.18, 0.17, 0.16, 0.22, 0.17} respectively for the regions I, IIa, IIb, III, IV, and V. The mean dTDP magnitudes for the surface and side lobes, estimated using the heuristically assigned directions as shown in Fig. 8, are provided in Table 1.

3.2.2. Reliability and reproducibility of dTDPs—Fig. 9 demonstrates the Pearson correlations within and between the CDMD and HHSD. Within group dTDP correlations were greater than 0.75 for 98%, 99%, and 97% of the total number of pairwise correlations respectively for HHSD-A, HHSD-B, and CDMD (Fig. 9a–c). We also observed that the correlations between the individuals of CDMD and HHSD-A were greater than 0.75 for 97% of the total number of pairwise correlations (Fig. 9d).

In the test-retest analysis, we used scans from six subjects from the CDMD, who had been scanned twice on the same day, to compare the dTDPs of each CC region between the consecutive scan sessions for each subject. Reproducibility was expressed as the respective Pearson correlations as provided in Table 2. The test-retest sessions had dTDPs for which the pairwise correlations were greater than 0.97 (Table 2).

We also evaluated the test-retest performance results for our CC parcellation scheme using the dice overlap score $(2(|X \cap Y|)/(|X| + |Y|))$ between the parcellated CC regions of two scans from the same subject. The dice scores were greater than 0.9 for most of the comparisons (Table 3).

3.2.3. Motion estimations—We also estimated head motion parameters using the eddy QC, as diffusion imaging measures can be affected by head motion during scanning (Bastiani et al., 2019). As shown in Fig. 10, both the HHSD-A and the CDMD (Tian et al., 2022) had less than 1 mm relative average motion, suggesting that the dTDP measures are not affected by subject motion.

4. Discussion

In this study, we used a novel algorithm, dTDP, to evaluate the directional characteristics of tract density patterns of distinct CC regions in healthy subjects. We found that our results provided an unbiased, reliable, and sensitive approach insensitive to variations in acquisition parameters and without the need for *a priori* assumptions of connectivity with topologically selective cortical regions. A major strength of this approach is that, unlike graph-based approaches, which provide a connectivity score between two regions (Rubinov and Sporns, 2010), dTDP interprets the interhemispheric connectivity across the entire structure and provides a directional density pattern at the macroscopic scale. dTDP is unique as, unlike orientation-independent shape features, such as the mean length (Schmied et al., 2020; Yeh, 2020), it utilizes probabilistic trajectory of an individual pathway and quantifies the density towards the directions starting from the mid-sagittal center of the CC region. Therefore, dTDP provides an orientation-dependent measure of interhemispheric connectivity.

This study is important for several reasons. As demonstrated, dTDP provides a distinct assessment information measure for interhemispheric connectivity with high reliability both within and across datasets. It also provides information without the need for *a priori* designations of cortical regions of interest, in contrast to prior connectivity studies, which have been considered cortical regions as seeds or targets (Liu et al., 2017; Mars et al., 2018). We also demonstrated that using an indirect approach, we could obtain information about interhemispheric connectivity representing both the density of fibers able to reach cortical regions (surface lobes) and the density of those that reached only mid-way (side lobes). In this way, our method is able to generate an estimate of the density of CC fibers as they turn/realign and merge with other bundles to run towards the cortical surface. This suggests that, using these dTDPs, it may be possible to monitor the structure of the crossing bending regions within the CC prior to reaching their cortical destination using standard diffusion acquisition parameters, something that cannot be accomplished with the current available methods.

Alterations in the white matter integrity and connectivity have been recognized as both prominent and significant in several neurodegenerative diseases including Alzheimer's, Parkinson's, and Huntington's disease (Nir et al., 2013; Wu et al., 2020; Rosas et al., 2010). Our results suggest that the dTDP might provide the needed sensitivity and reliability to be of use in clinical applications, including age- or disease-related changes in interhemispheric architecture, providing opportunities to detect early pathological change. Additional future work will be required to fully explore the applicability of this approach to neurodegeneration in both cross-sectional and longitudinal analyses.

4.1. Limitations

As tractography provides an ill-posed solution to estimate the anatomical structure of the whole-brain white matter fiber trajectories, it may be prone to inconsistent reconstructions, mostly identified as false-positive fibers, which are often discarded when using region sensitive filtering operations (Maffei et al., 2021). Since dTDP is reconstructed by carefully seeding the tractography from the mid-sagittal CC, the existence of false-positive connections is a less likely concern. Instead, false positive fibers could instead represent an indicator of damaged connections in clinical applications, but this requires additional evaluation.

Since the dTDP framework does not require identification of a specific cortical target regions, the proposed framework provides a course end region analysis. However, we should note that the uncertainty of the fibers is greatest at target/cortical surface regions (Behrens et al., 2003; Friman and Westin, 2005), which is an issue for all tractography applications. This is because tractography streamlines have branching fibers along the commissural pathway closer to the surface, where tractography is known to be biased (Schilling et al., 2018). By projecting the tract densities on an optimal plane to reflect only directional density of the fibers along the dominant directions of CC (left to right), we aimed to partially reduce the branching bias.

5. Conclusion

In this study, we developed a novel algorithm to evaluate interhemispheric connectivity of regionally selective regions of CC, that provides information about different locations along the callosal trajectory. Variability and reproducibility experiments performed using two human datasets suggest that this method is sensitive, reliable, and reproducible, and support its use in clinical applications to evaluate interhemispheric connectivity.

Acknowledgments

Funding for this research provided by: the National Institutes of Health R01:NS106384 and R01:NS114562.

We are grateful Dr. Qiyuan Tian and Dr. Susie Y. Huang for providing the demographics information. We also thank Dr. Shahin Nasr for scientific feedback and editorial comments.

Data availability

The original contributions presented in the study are included in the article, further inquiries can be directed to the authors. The code and compiled binaries will be available to public.

Appendix A.: CC centerline curve fitting algorithm

Algorithm 1.

Centerline CC curve reconstruction

Require: Fractional anisotropy map, $FA : \mathbb{R}^3 \rightarrow \mathbb{R}$; Principle direction of diffusion tensor map, $V1 : \mathbb{R}^3 \rightarrow \mathbb{R}^3$ Freesurfer reconstruction of $CC, CC_{recon}: \mathbb{R}^3 \rightarrow \mathbb{R}$ Anterior CC landmark, $\overrightarrow{c_1} \in \mathbb{R}^3$ Posterior CC landmark, $\overrightarrow{c_n} \in \mathbb{R}^3$; 3D vector dimensions [Left-to-Right,Anterior-to-Posterior, Foot-to-Head].

(Note that principal direction of diffusion tensor (V1) and fractional anisotropy (FA) maps were reconstructed in MNI152 space particularly for this step. $\overrightarrow{d_i}$ parameterized using the tangent vectors of a partial 2D ellipse $(\frac{dy}{dt} = \cos(t), \frac{dx}{dt} = -3\sin(t)$, and $t \in \{9\pi/8, \ldots, 0\})$.)

$\overrightarrow{v} \leftarrow \overrightarrow{c_n} - \overrightarrow{c_1}$; $CC_{curve} \leftarrow \{\overrightarrow{c_1}\}$; REACHED $\leftarrow$ false;

while REACHED $\neq$ true **do**

$\overrightarrow{c_i} \leftarrow$ last voxel added to the list CC_{curve}; $\overrightarrow{s_i} \leftarrow \overrightarrow{c_i} - \overrightarrow{c_1}$;

$t_i \leftarrow (9\pi/8)(1 - \frac{\| \overrightarrow{s_i} \|}{\| \overrightarrow{v} \|})$

$\overrightarrow{d_i} \leftarrow [0, 3\sin(t_i), \quad -\cos(t_i)]$

$\mathcal{N} \leftarrow \{\}; \mathcal{N}_{all} \leftarrow \{[0, -1, -1], [0, 0, -1], [0, -1, 0], [0, 0, 1], [0, 1, 0], [0, 1, 1]\}$;

for all $\overrightarrow{n} \in \mathcal{N}_{all}$ **do**

if $\langle \overrightarrow{d_i}, \overrightarrow{n} \rangle > 0.0$ **then**

$\mathcal{N} \leftarrow \{\mathcal{N}, \overrightarrow{n}\}$;

end if

end for

$\overrightarrow{n_i} \leftarrow [0, 0, 0]$

for all $\overrightarrow{n} \in \mathcal{N}$ **do**

if $\overrightarrow{c_i} + \overrightarrow{n} == \overrightarrow{c_n}$ **then**

$\overrightarrow{n_i} \leftarrow \overrightarrow{n}$; REACHED ← true; **break;**

end if

$$\mathcal{R} \leftarrow \frac{5.0}{\|\overrightarrow{d_i}\|}\left(\frac{\langle \overrightarrow{d_i}, \overrightarrow{n}\rangle}{\|\overrightarrow{d_i}\| \, \|\overrightarrow{n}\|}\right)$$

$$\omega \leftarrow \mathrm{CC}_{\mathrm{recon}}(\overrightarrow{c_i} + \overrightarrow{n})\mathrm{FA}(\overrightarrow{c_i} + \overrightarrow{n})\langle \mathrm{V}\,1(\overrightarrow{c_i} + \overrightarrow{n}), [1,0,0]\rangle + \mathcal{R}$$

if $\omega > \rho$ **then**

$\overrightarrow{n_i} \leftarrow \overrightarrow{n}$

end if

end for

$$\mathrm{CC}_{\mathrm{curve}} \leftarrow \{\mathrm{CC}_{\mathrm{curve},}(\overrightarrow{c_i} + \overrightarrow{n_i})\}$$

end while

Abbreviations:

CC	Corpus callosum
dTDP	Directional tract density pattern
MRI	Magnetic resonance imaging
FA	Fractional anisotropy
AD	Axial diffusivity
RD	Radial diffusivity
QCD	Quartile coefficient of dispersion
HHSD	Healthy human subjects dataset
CDMD	Comprehensive diffusion MRI dataset
FOD	Fiber orientation distribution

References

Amunts K, Mohlberg H, Bludau S, Zilles K, 2020. Julich-brain: a 3d probabilistic atlas of the human brain's cytoarchitecture. Science 369, 988–992. 10.1126/science.abb4588. [PubMed: 32732281]

Andersson JL, Sotiropoulos SN, 2016. An integrated approach to correction for off-resonance effects and subject movement in diffusion MR imaging. Neuroimage 125, 1063–1078. 10.1016/j.neuroimage.2015.10.019. [PubMed: 26481672]

Andersson JLR, Graham MS, Zsoldos E, Sotiropoulos SN, 2016. Incorporating outlier detection and replacement into a non-parametric framework for movement and distortion correction of diffusion MR images. Neuroimage 141, 556–572. 10.1016/j.neuroimage.2016.06.058. [PubMed: 27393418]

Basser PJ, Pierpaoli C, 1996. Microstructural and physiological features of tissues elucidated by quantitative-diffusion-tensor MRI. J. Magn. Reson., Ser. B 111, 209–219. 10.1006/jmrb.1996.0086. [PubMed: 8661285]

Bastiani M, Cottaar M, Fitzgibbon SP, Suri S, Alfaro-Almagro F, Sotiropoulos SN, Jbabdi S, Andersson JL, 2019. Automated quality control for within and between studies diffusion MRI data using a non-parametric framework for movement and distortion correction. Neuroimage 184, 801–812. 10.1016/j.neuroimage.2018.09.073. [PubMed: 30267859]

Behrens T, Woolrich M, Jenkinson M, Johansen-Berg H, Nunes R, Clare S, Matthews P, Brady J, Smith S, 2003. Characterization and propagation of uncertainty in diffusion-weighted MR imaging. Magn. Reson. Med. 50, 1077–1088. 10.1002/mrm.10609. [PubMed: 14587019]

Bonett DG, 2006. Confidence interval for a coefficient of quartile variation. Comput. Stat. Data Anal. 50, 2953–2957. 10.1016/j.csda.2005.05.007.

Calamante F, Tournier JD, Jackson GD, Connelly A, 2010. Track-density imaging (TDI): super-resolution white matter imaging using whole-brain track-density mapping. Neuroimage 53, 1233–1243. 10.1016/j.neuroimage.2010.07.024. [PubMed: 20643215]

Caruyer E, Daducci A, Descoteaux M, Houde JC, Thiran JP, Verma R, 2014. Phantomas: a Flexible Software Library to Simulate Diffusion MR Phantoms. ISMRM, Milan, Italy.

Dhollander T, Mito R, Raffelt D, Connelly A, 2019. Improved white matter response function estimation for 3-tissue constrained spherical deconvolution. In: Proceedings of the International Society for Magnetic Resonance in Medicine. Abstract number 555.

Emsell L, Adamson C, De Winter FL, Billiet T, Christiaens D, Bouckaert F, Adamczuk K, Vandenberghe R, Seal ML, Sienaert P, Sunaert S, Vandenbulcke M, 2017. Corpus callosum macro and microstructure in late-life depression. J. Affect. Disord. 222, 63–70. 10.1016/j.jad.2017.06.063. [PubMed: 28672181]

Friman O, Westin CF, 2005. Uncertainty in white matter fiber tractography. In: Duncan JS, Gerig G (Eds.), Medical Image Computing and Computer-Assisted Intervention – MICCAI 2005. Springer Berlin Heidelberg, Berlin, Heidelberg, pp. 107–114. 10.1007/11566465_14.

Greve DN, Fischl B, 2009. Accurate and robust brain image alignment using boundary-based registration. Neuroimage 48, 63–72. 10.1016/j.neuroimage.2009.06.060. [PubMed: 19573611]

Hofer S, Frahm J, 2006. Topography of the human corpus callosum revisited—comprehensive fiber tractography using diffusion tensor magnetic resonance imaging. Neuroimage 32, 989–994. 10.1016/j.neuroimage.2006.05.044. [PubMed: 16854598]

Huang SY, Fan Q, Machado N, Eloyan A, Bireley JD, Russo AW, Tobyne SM, Patel KR, Brewer K, Rapaport SF, Nummenmaa A, Witzel T, Sherman JC, Wald LL, Klawiter EC, 2019. Corpus callosum axon diameter relates to cognitive impairment in multiple sclerosis. Annals of Clinical and Translational Neurology 6, 882–892. 10.1002/acn3.760. 10.1002/acn3.760. [PubMed: 31139686]

Jenkinson M, Beckmann CF, Behrens TE, Woolrich MW, Smith SM, 2012. Fsl. NeuroImage 62, 782–790. 10.1016/j.neuroimage.2011.09.015. [PubMed: 21979382]

Jeurissen B, Tournier JD, Dhollander T, Connelly A, Sijbers J, 2014. Multi-tissue constrained spherical deconvolution for improved analysis of multi-shell diffusion MRI data. Neuroimage 103, 411–426. 10.1016/j.neuroimage.2014.07.061. [PubMed: 25109526]

Kingsley PB, 2006. Introduction to diffusion tensor imaging mathematics: Part II. anisotropy, diffusion-weighting factors, and gradient encoding schemes. Concepts Magn. Reson. 28A, 123–154. 10.1002/cmr.a.20049.

Liu K, Zhang T, Chu WC, Mok VC, Wang D, Shi L, 2017. Group comparison of cortical fiber connectivity map: an application between post-stroke patients and healthy subjects. Neuroscience 344, 15–24. 10.1016/j.neuroscience.2016.12.026. [PubMed: 28039039]

Maffei C, Lee C, Planich M, Ramprasad M, Ravi N, Trainor D, Urban Z, Kim M, Jones R, Henin A, Hofmann S, Pizzagalli D, Auerbach R, Gabrieli J, Whitfield-Gabrieli S, Greve D, Haber S, Yendiki A, 2021. Using diffusion MRI data acquired with ultra-high gradient strength to improve tractography in routine-quality data. Neuroimage 245, 118706. 10.1016/j.neuroimage.2021.118706. [PubMed: 34780916]

Mars RB, Sotiropoulos SN, Passingham RE, Sallet J, Verhagen L, Khrapitchev AA, Sibson N, Jbabdi S, 2018. Whole brain comparative anatomy using connectivity blueprints. Elife 7, e35237. 10.7554/eLife.35237. [PubMed: 29749930]

Mazziotta JC, Toga AW, Evans A, Fox PT, Lancaster JL, Zilles K, Woods RP, Paus T, Simpson G, Pike B, Holmes CJ, Collins L, Thompson PM, MacDonald D, Iacoboni M, Schormann T, Amunts K, Palomero-Gallagher N, Geyer S, Parsons L, Narr KL, Kabani NJ, Goualher GL, Boomsma DI, Cannon TD, Kawashima R, Mazoyer B, 2001. A probabilistic atlas and reference system for the human brain: international consortium for brain mapping (ICBM). Phil. Trans. Roy. Soc. Lond. B Biol. Sci. 356, 1293–1322. 10.1098/rstb.2001.0915. [PubMed: 11545704]

Münch M, Müller HP, Behler A, Ludolph AC, Kassubek J, 2022. Segmental alterations of the corpus callosum in motor neuron disease: a DTI and texture analysis in 575 patients. Neuroimage: Clinical 35, 103061. 10.1016/j.nicl.2022.103061. [PubMed: 35653913]

Mori S, Crain BJ, 2005. MRI Atlas of Human White Matter, first ed. Elsevier, Amsterdam; Boston.

Nir TM, Jahanshad N, Villalon-Reina JE, Toga AW, Jack CR, Weiner MW, Thompson PM, 2013. Effectiveness of regional DTI measures in distinguishing alzheimer's disease, MCI, and normal aging. Neuroimage: Clinical 3, 180–195. 10.1016/j.nicl.2013.07.006. [PubMed: 24179862]

Rosas HD, Lee SY, Bender AC, Zaleta AK, Vangel M, Yu P, Fischl B, Pappu V, Onorato C, Cha JH, Salat DH, Hersch SM, 2010. Altered white matter microstructure in the corpus callosum in huntington's disease: implications for cortical "disconnection.". Neuroimage 49, 2995–3004. 10.1016/j.neuroimage.2009.10.015. [PubMed: 19850138]

Rubinov M, Sporns O, 2010. Complex network measures of brain connectivity: uses and interpretations. Neuroimage 52, 1059–1069. 10.1016/j.neuroimage.2009.10.003. [PubMed: 19819337]

Rusina R, Bajtosova R, Cséfalvay Z, Keller J, Kavkova A, Kukal J, Matej R, 2022. Comorbid neurodegeneration in primary progressive aphasia: clinicopathological correlations in a single-center study. Behav. Neurol, 6075511 10.1155/2022/6075511. [PubMed: 36120397]

Russo AW, Stockel KE, Tobyne SM, Ngamsombat C, Brewer K, Nummenmaa A, Huang SY, Klawiter EC, 2022. Associations between corpus callosum damage, clinical disability, and surface-based homologous inter-hemispheric connectivity in multiple sclerosis. Brain Struct. Funct. 227, 2909–2922. 10.1007/s00429-022-02498-7. [PubMed: 35536387]

Schilling K, Gao Y, Janve V, Stepniewska I, Landman BA, Anderson AW, 2018. Confirmation of a gyral bias in diffusion MRI fiber tractography. Hum. Brain Mapp. 39, 1449–1466. 10.1002/hbm.23936. [PubMed: 29266522]

Schilling KG, Nath V, Hansen C, Parvathaneni P, Blaber J, Gao Y, Neher P, Aydogan DB, Shi Y, Ocampo-Pineda M, Schiavi S, Daducci A, Girard G, Barakovic M, Rafael-Patino J, Romascano D, Rensonnet G, Pizzolato M, Bates A, Fischi E, Thiran JP, Canales-Rodríguez EJ, Huang C, Zhu H, Zhong L, Cabeen R, Toga AW, Rheault F, Theaud G, Houde JC, Sidhu J, Chamberland M, Westin CF, Dyrby TB, Verma R, Rathi Y, Irfanoglu MO, Thomas C, Pierpaoli C, Descoteaux M, Anderson AW, Landman BA, 2019. Limits to anatomical accuracy of diffusion tractography using modern approaches. Neuroimage 185, 1–11. 10.1016/j.neuroimage.2018.10.029. [PubMed: 30317017]

Schmied A, Soda T, Gerig G, Styner M, Swanson MR, Elison JT, Shen MD, McKinstry RC, Pruett JR, Botteron KN, Estes AM, Dager SR, Hazlett HC, Schultz RT, Piven J, Wolff JJ, 2020. Sex differences associated with corpus callosum development in human infants: a longitudinal multimodal imaging study. Neuroimage 215, 116821. 10.1016/j.neuroimage.2020.116821. [PubMed: 32276067]

Stezin A, Reddam V, Hegde S, Yadav R, Saini J, Pal P, 2021. Morphometric mapping of the macrostructural abnormalities of midsagittal corpus callosum in wilson's disease. Annals of Movement Disorders 4, 60–65. 10.4103/AOMD.AOMD_41_20. [PubMed: 35936213]

Tian Q, Fan Q, Witzel T, Polackal MN, Ohringer NA, Ngamsombat C, Russo AW, Machado N, Brewer K, Wang F, Setsompop K, Polimeni JR, Keil B, Wald LL, Rosen BR, Klawiter EC, Nummenmaa A, Huang SY, 2022. Comprehensive diffusion MRI dataset for in vivo human brain microstructure mapping using 300 mT/m gradients. Sci. Data 9. 10.1038/s41597-021-01092-6. Article number 7.

Tournier JD, Calamante F, Connelly A, 2007. Robust determination of the fibre orientation distribution in diffusion MRI: non-negativity constrained super-resolved spherical deconvolution. Neuroimage 35, 1459–1472. 10.1016/j.neuroimage.2007.02.016. [PubMed: 17379540]

Tournier JD, Calamante F, Gadian DG, Connelly A, 2010. Improved probabilistic streamlines tractography by 2nd order integration over fibre orientation distributions. In: Proceedings of the International Society for Magnetic Resonance in Medicine. Abstract number 1670.

Veraart J, Novikov DS, Christiaens D, Ades-aron B, Sijbers J, Fieremans E, 2016. Denoising of diffusion MRI using random matrix theory. Neuroimage 142, 394–406. 10.1016/j.neuroimage.2016.08.016. [PubMed: 27523449]

Watanabe A, Nakamae T, Sakai Y, Nishida S, Abe Y, Yamada K, Yokota I, Narumoto J, 2018. The detection of white matter alterations in obsessive-compulsive disorder revealed by TRActs Constrained by UnderLying Anatomy (TRACULA). Neuropsychiatric Dis. Treat. 14, 1635–1643. 10.2147/NDT.S164058.

Wu J, Guo T, Zhou C, Guan X, Gao T, Xuan M, Gu Q, Huang P, Song Z, Pu J, Yan Y, Tian J, Zhang B, Xu X, Zhang M, 2020. Longitudinal macro/microstructural alterations of different callosal subsections in Parkinson's disease using connectivity-based parcellation. Front. Aging Neurosci. 12 10.3389/fnagi.2020.572086.

Xu L, Chang SH, Yang L, Zhang LJ, 2021. Quantitative evaluation of callosal abnormalities in relapsing-remitting multiple sclerosis using diffusion tensor imaging: a systemic review and meta-analysis. Clin. Neurol. Neurosurg. 201, 106442 10.1016/j.clineuro.2020.106442. [PubMed: 33373835]

Yeh FC, 2020. Shape analysis of the human association pathways. Neuroimage 223, 117329. 10.1016/j.neuroimage.2020.117329. [PubMed: 32882375]

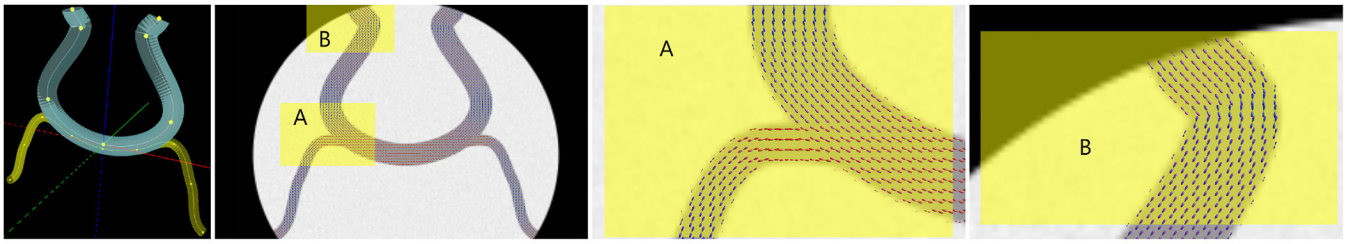

(a) Control points. (b) Fiber orientation distributions. (c) Zoomed view of the side region. (d) Zoomed view of the surface region.

Fig. 1.

Synthetic CC data created using a preset multi-shell scheme, 2 mm voxel resolution, and 8 mm bundle radius: (a) Yellow points demarcates control points used to reconstruct a tubular structure of the CC, and (b–d) demonstrate orientations of the reconstructed fibers along the structure. Yellow regions A and B showed in (b) are zoomed in (c) and (d).

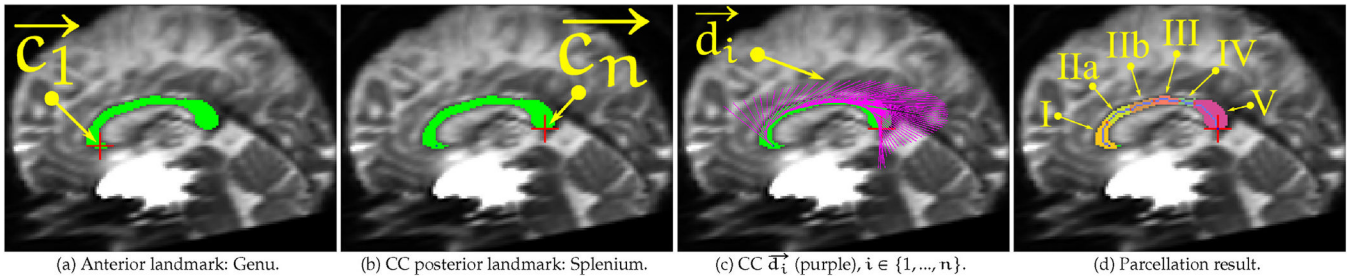

(a) Anterior landmark: Genu. (b) CC posterior landmark: Splenium. (c) CC $\vec{d_i}$ (purple), $i \in \{1, ..., n\}$. (d) Parcellation result.

Fig. 2.
Parcellation of CC for a healthy subject.

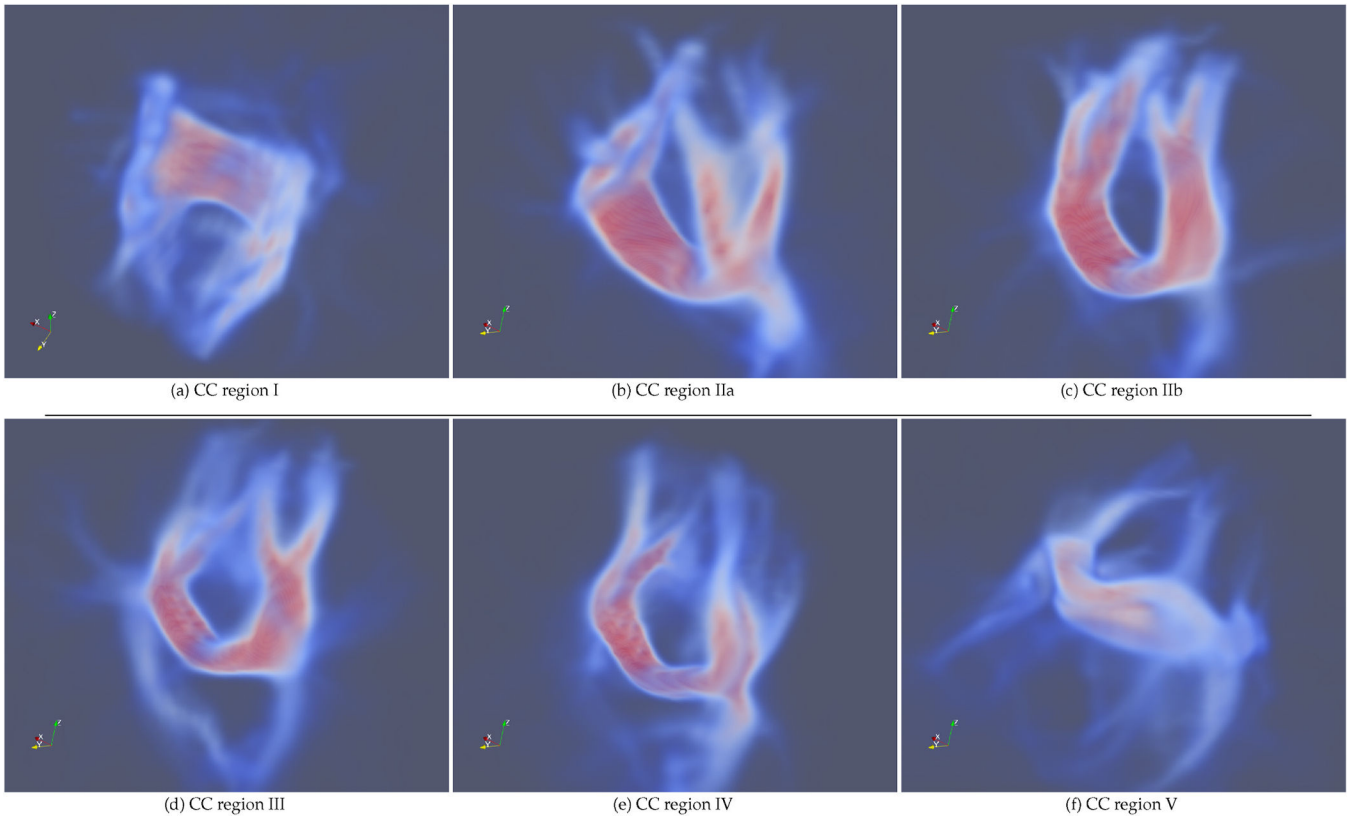

Fig. 3.

Volume rendering of tract densities traversing each CC region for a healthy human subject. The 3D directions X shows the right, Y shows the anterior, and Z shows the superior directions.

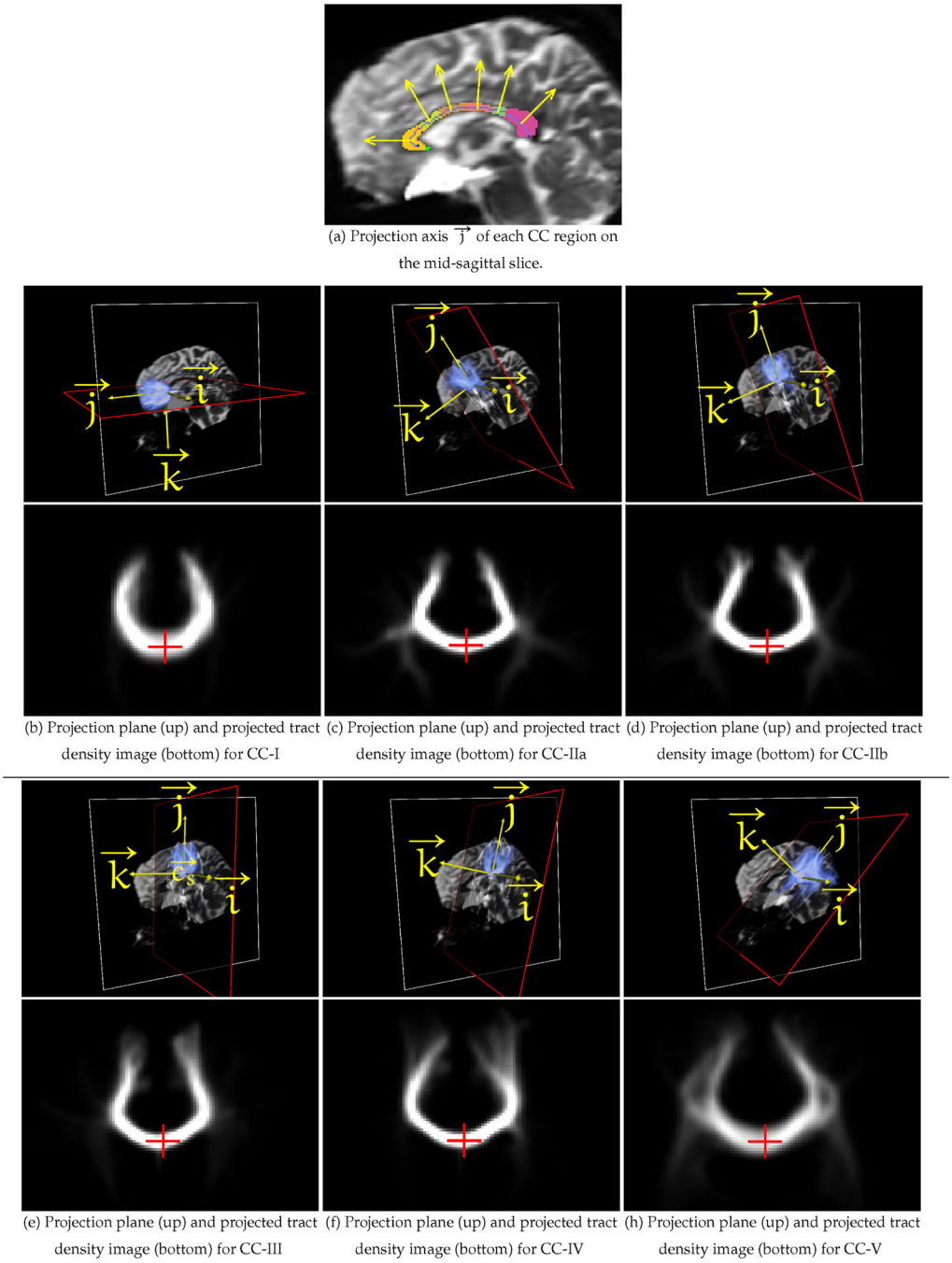

Fig. 4.

The CC subdivision given in (a) shows the axis $\vec{j}$ on mid-sagittal view, whereas the projection planes, defined using $\vec{i}$ and $\vec{j}$ (red frame), are shown on upper images of (b–h) together with the corresponding projected tract densities, $I(\vec{X}_{(a,b)})$ in the bottom images, where the red cross shows $\vec{c}_s$.

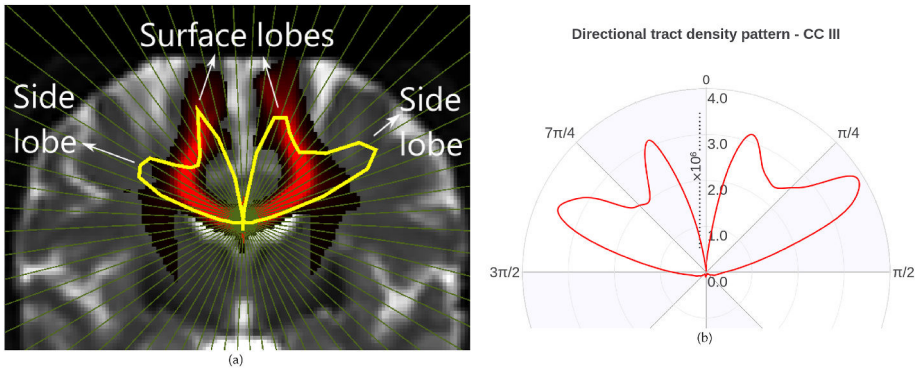

Fig. 5.

dTDP of CC region III from a healthy human subject shows: (a) the angular parcellation of the region (green lines) together with the yellow curve depicting the dTDP, $Q(k\alpha)$, the sum of tract densities along each angular portion $(k\alpha)$ of the projection image $(I(\overrightarrow{X}_{(a,b)}))$, where $\overrightarrow{c}_s$ is at the origin of the coordinate space (the background is sliced mean b0 image at the projection plane). (b) the dTDP (red curve) on the polar coordinate space in order to demonstrate the directional density magnitudes.

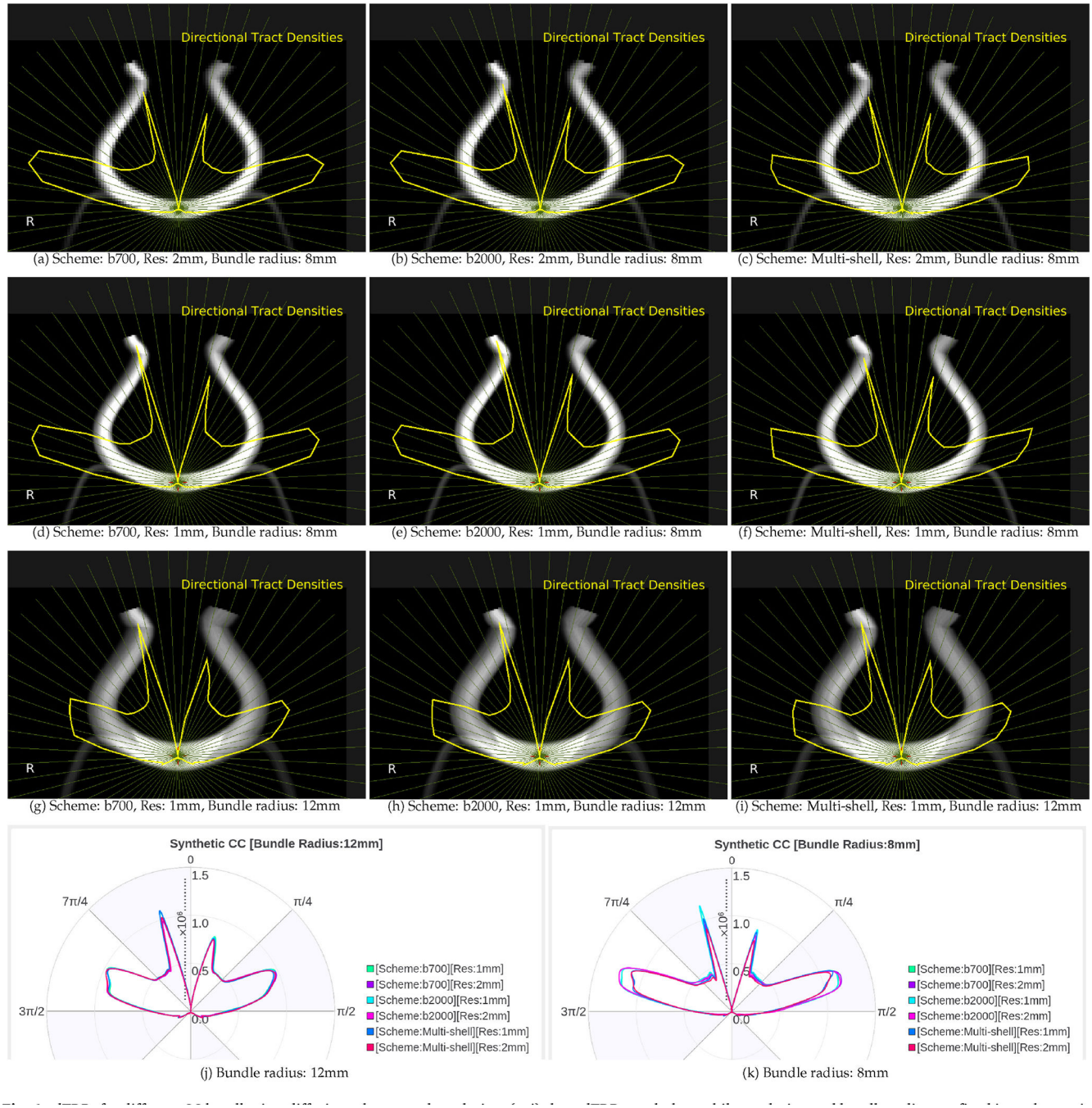

Fig. 6.

dTDPs for different CC bundle size, diffusion scheme, and resolution. (a–i) show dTDPs, such that, while resolution and bundle radius are fixed in each row, in columns left to right, dTDPs for b700, b2000, and multi-shell schemes are depicted (background image is the projection of tract densities). The first and second rows compare different resolutions (1 and 2 mm), and the second and third rows compare the bundle radius of 12 and 8 mm. (j–h) overlays all dTDPs separately for bundle sizes of 12 mm and 8 mm.

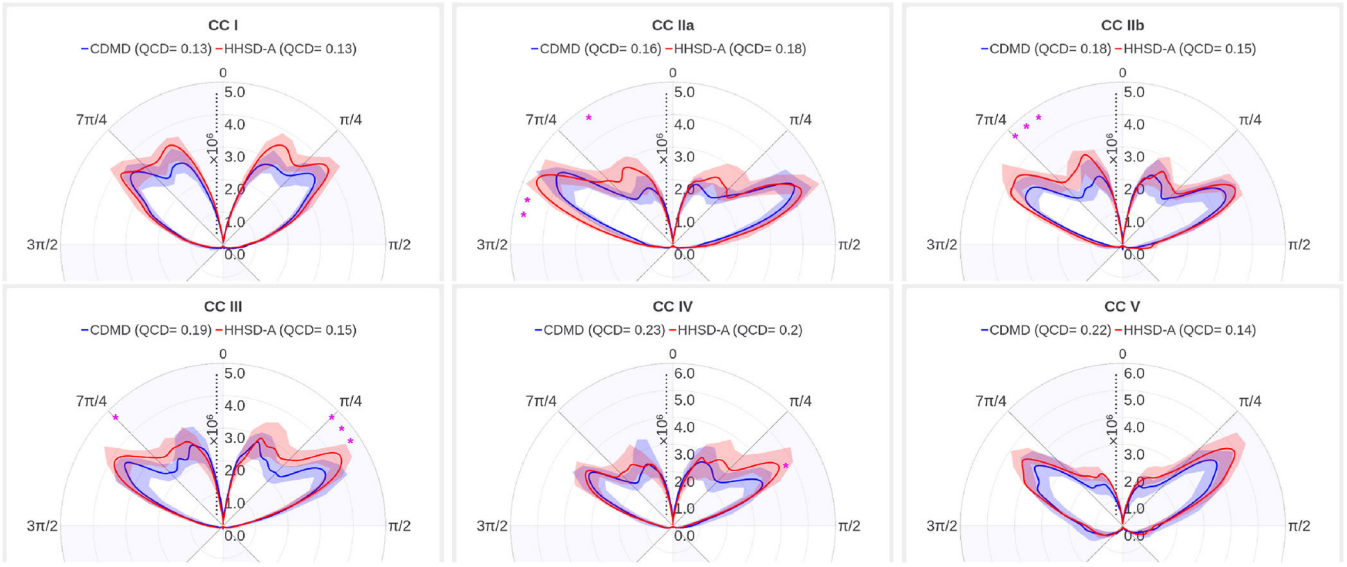

Fig. 7.

Comparison of directional tract density patterns (dTDPs) between CDMD (blue) and HHSD-A (red) for each CC region. The datasets were not significantly different from each other noting that a few number of "*" symbols demonstrate sparse/inadequate directions of difference ($p < 0.05$) at the end of the radial axis.

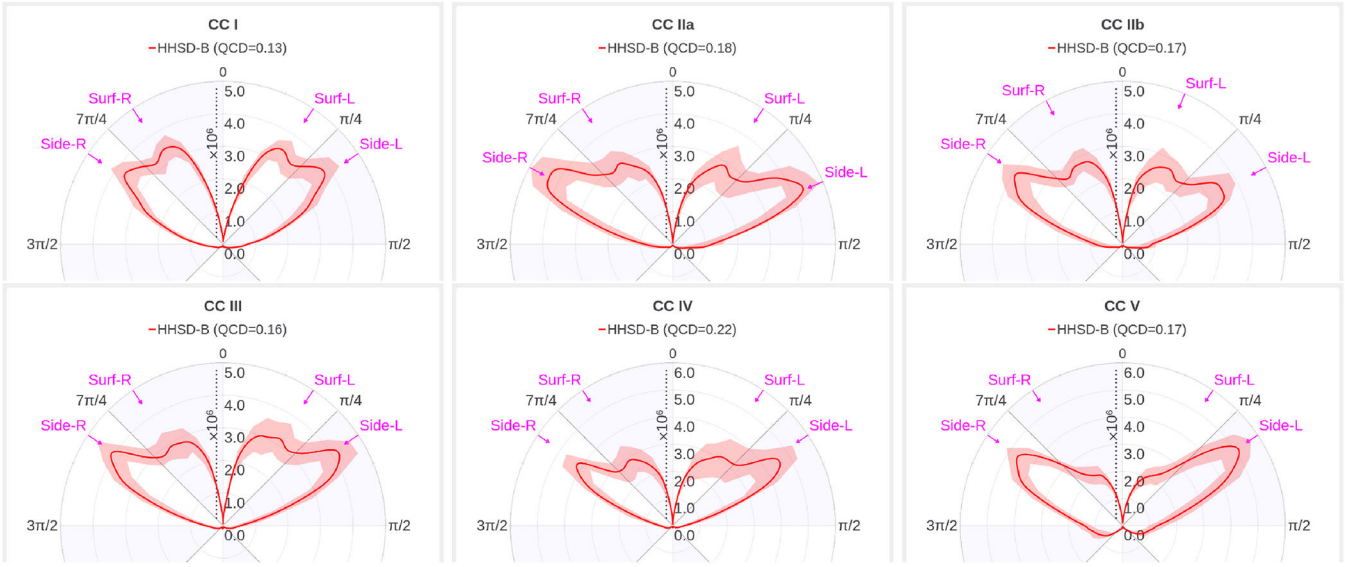

Fig. 8.

Directional tract density patterns for the CC regions in the HHSD-B cohort, depicting heuristically assigned principal directions for the surface and side lobes (L: Left, R: Right, Surf: surface lobe, Side: side lobe) and the variability in the dataset for each direction (shaded region).

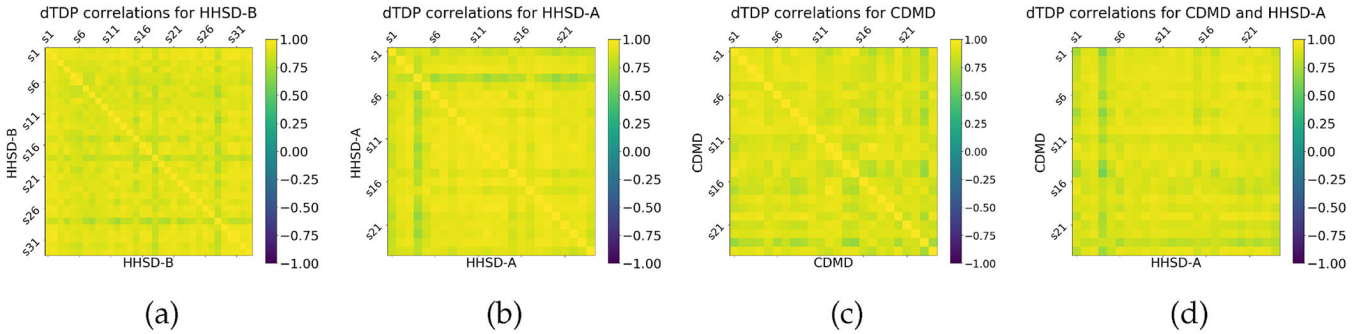

Fig. 9.

Correlation matrices of the HHSD and CDMD datasets. (a–c) show the between subject correlations of individual dTDPs in the datasets ((a) HSSD-A, (b) HHSD-B, and (c) CDMD). (d) demonstrates the correlation between CDMD and HHSD-A. In all cases, correlation coefficients were greater than 0.75 for at least 97% of total number of pairwise correlations, demonstrating excellent within and between dataset reliability. We used *viridis* color palette: dark blue (−1.0) to yellow (1.0) from python matplotlib package in color bar showing high correlations in yellow.

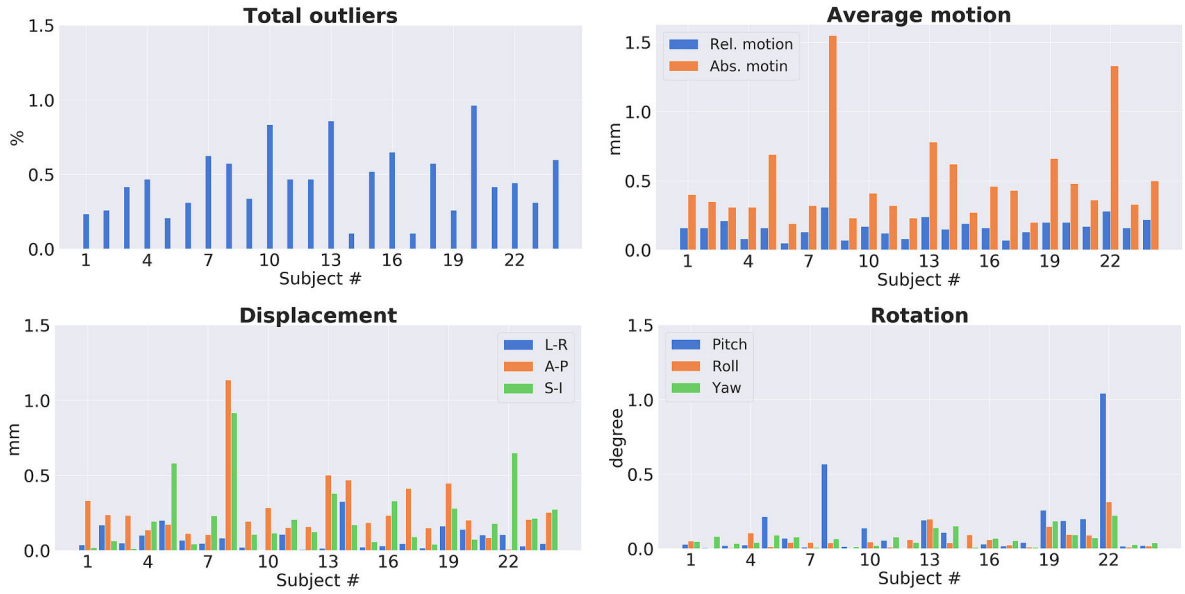

Fig. 10.

Head stability during the diffusion acquisition for all the subjects in HHSD-A: Total outliers were shown to reveal the percentage of dropout slices detected in diffusion data. Individual head motion parameters were also shown with average motion, rotation, and displacement in all dimensions.

Table 1

dTDP variability of HHSD-B: Directional tract densities (mean ± standard deviation) for the side and surface lobes marked in Fig. 8. Density values are given on the order of 10^6.

CC region	Side-Right	Surface-Right	Surface-Left	Side-Left
I	3.65 ± 0.59	3.40 ± 0.58	3.41 ± 0.55	3.76 ± 0.61
IIa	4.32 ± 0.91	2.97 ± 0.71	2.89 ± 0.87	4.34 ± 0.90
IIb	3.91 ± 0.91	2.79 ± 0.60	2.53 ± 0.69	3.47 ± 0.71
III	4.07 ± 0.83	2.90 ± 0.67	3.19 ± 0.64	4.16 ± 0.90
IV	4.14 ± 0.94	2.89 ± 0.80	3.06 ± 1.07	4.45 ± 1.24
V	4.62 ± 0.80	2.24 ± 0.51	2.25 ± 0.63	5.11 ± 0.93

Table 2

Test-retest reproducibility of the dTDP. S-# shows the subject index.

CC region	S-1	S-2	S-3	S-4	S-5	S-6	Mean ± Std
I	0.999	0.991	0.998	0.997	0.992	0.998	0.993±0.009
IIa	0.998	0.984	0.984	0.962	0.990	0.992	0.980±0.021
IIb	0.999	0.986	0.997	0.979	0.979	0.998	0.989±0.009
III	0.995	0.987	0.999	0.986	0.982	0.999	0.990±0.008
IV	0.989	0.985	0.999	0.975	0.988	0.996	0.984±0.014
V	0.999	0.985	0.998	0.988	0.992	0.999	0.993±0.006

Table 3

Dice scores of CC parcellation for the subjects with repeated scans.

CC region	S-1	S-2	S-3	S-4	S-5	S-6
I	0.968	0.889	0.960	0.914	0.966	0.943
IIa	0.942	0.800	0.964	0.807	0.966	0.939
IIb	0.949	0.867	0.942	0.814	0.924	0.985
III	0.904	0.900	0.939	0.853	0.926	0.945
IV	0.846	0.780	0.969	0.773	0.938	0.939
V	0.946	0.902	0.981	0.910	0.966	0.955